MERCK

catch the SUN

Product Category list:

- Organic Photovoltaic (OPV) Donors and Acceptors
- Dye-Sensitized Solar Cell Materials
- Perovskite Materials

Visit us at:
SigmaAldrich.com/organic-electronics

MK_AD9792EN 43729 08/2022

The Life Science business of Merck operates as MilliporeSigma in the U.S. and Canada.

Sigma-Aldrich®
Lab & Production Materials

ADVANCED ENERGY MATERIALS
www.advenergymat.de

Electrochemical Performance Enhancement of 3D Printed Electrodes Tailored for Enhanced Gas Evacuation during Alkaline Water Electrolysis

*Fernando Rocha, Renaud Delmelle, Christos Georgiadis, and Joris Proost**

A zero-gap cell with porous electrodes is a promising configuration for alkaline water electrolysis. However, gas evacuation becomes a challenge in that case, as bubbles can get trapped within the electrode's 3D structure. This work considers a number of 3D printed electrode geometries with so-called triply periodic minimal surfaces (TPMS). The latter is a mathematically defined structure that repeats itself in three dimensions with zero mean curvature, and can therefore be expected to be particularly well-suited to enhance gas evacuation. Another advantage as compared to other state-of-the-art 3D electrodes like foams or felts lies in the fact that their porosity, which determines the available surface area, and their pore size or flow channel dimensions, which determines the degree of bubble entrapment, can be varied independently. By a combined experimental and modeling approach, this work then identifies the structural parameters that direct the performance of such 3D printed TPMS geometries toward enhanced gas evacuation. It is demonstrated that an optimal combination of these parameters allows, under a forced electrolyte flow, for a reduction in cell overpotential of more than 20%. This indicates that efforts in optimizing the electrode's geometry can give a similar electrochemical performance enhancement as optimizing its electro-catalytic composition.

1. Introduction

In 2020, 88.5 Mt of hydrogen were produced worldwide for different industrial applications: 42% for oil refining, 38% for ammonia production, 15% for methanol, and 5% for direct reduced iron. Unfortunately, 99.4% of this hydrogen was produced from fossil fuels, resulting in the emission of 900 Mt of carbon dioxide.[1] One of the strategies to decarbonize this industry is to produce hydrogen by water electrolysis using renewable electricity. This promising method allows not only to decarbonize the current hydrogen production but to decarbonize other industries as well since the carbon-free electrolytic hydrogen (or derivatives) can replace fossil fuels in the transport and heating sectors as well. As a consequence, the International Energy Agency estimates a 140% growth in hydrogen demand by 2030, with water electrolysis being responsible for almost 40% of the total production.[1]

There are three main water electrolysis technologies. The most mature one is alkaline water electrolysis (AWE), with a market share of ≈60%, followed by proton exchange membrane water electrolysis (≈30% market share), and solid oxide water electrolysis.[1,2] Besides being the most mature method, AWE also has the lowest capital cost (€/kW) at a given power input,[3] since it uses abundant and inexpensive materials.[4]

The state-of-the-art AWE cell configuration is a zero-gap assembly. In this configuration, the electrodes, in general 2D electrodes such as perforated plates, expanded metals, or meshes, are pressed against a separator with a thickness on the order of hundreds of micrometers.[5] Recently, 3D electrode geometries such as foams and felts have been used with promising results,[6] especially when a forced electrolytic flow is imposed.[7] However, due to the stochastic nature of these geometries, gas removal may not be optimal. As an example, Kou et al. observed an enhancement in gas evacuation when replacing foams with periodic 3D structures.[8]

An important method to build tailored 3D periodic metallic structures is additive manufacturing using laser beam melting (LBM), also known as selective laser melting (SLM).[9] In this process, a thin layer of powder is deposited over a substrate plate or on the previously deposited layer and a laser beam melts the powder particles selectively. To avoid oxygen contamination, the process is done in a closed chamber containing an inert gas.[10] With the almost unlimited possible geometries that it allows to fabricate, it is important to find generic guidelines as to what kind of structure presents the best electrolytic performance in view of enhanced gas removal.

Recently, a study of membrane distillation for desalination has successfully shown that 3D printed spacers can enhance heat and mass transfer and reduce the formation of dead zones.[11]

F. Rocha, R. Delmelle, C. Georgiadis, J. Proost
Division of Materials and Process Engineering
Université catholique de Louvain
1348 Louvain-la-Neuve, Belgium
E-mail: joris.proost@uclouvain.be

The ORCID identification number(s) for the author(s) of this article can be found under https://doi.org/10.1002/aenm.202203087.

DOI: 10.1002/aenm.202203087

The novelty of that work was the use of mathematically developed triply periodic minimal surfaces (TPMS) as feed spacers. A TPMS is a mathematically defined structure that repeats itself in three dimensions with zero mean curvature.[12] Later, these spacers were tested for reverse osmosis and ultrafiltration, showing not only an enhancement in the mass transfer but also a reduction in fouling when compared with commercial stochastically structured spacers.[13] Following these observations, the present study aims at the analysis of different TPMS electrode geometries for AWE in view of enhanced gas evacuation. Three geometries were studied: Gyroid, Fischer–Koch, and Schwarz. They are described by the following structural equations:

Gyroid

$$t = \cos(g\cdot x)\cdot\sin(g\cdot y) + \cos(g\cdot y)\cdot\sin(g\cdot z) + \cos(g\cdot z)\cdot\sin(g\cdot x) \quad (1)$$

Fischer–Koch

$$t = \cos(2\cdot g\cdot x)\cdot\cos(g\cdot z)\cdot\sin(g\cdot y) + \cos(g\cdot x)\cdot\cos(2\cdot g\cdot y)\cdot\sin(g\cdot z) + \cos(g\cdot y)\cdot\cos(2\cdot g\cdot z)\cdot\sin(g\cdot x) \quad (2)$$

Schwarz

$$t = \sin(g\cdot z)\cdot\sin(g\cdot x) - 0.4\cdot\sin(1.2\cdot g\cdot y)\cdot\cos(g\cdot z)\cdot\cos(g\cdot x) \quad (3)$$

with

$$g = \frac{2\cdot\pi}{L} \quad (4)$$

In these equations, the lattice size L determines the periodicity and the parameter t is directly related to the porosity, as will be further illustrated below. It is already worth noticing that while Gyroidal and Fischer–Koch type electrodes have the same symmetry in all directions, Schwarz-shaped electrodes have a different symmetry for the vertical (y) direction. An example of each of these three geometries is shown in **Figure 1**. For the experiments, the electrolyte will be forced to flow vertically, parallel to the channels inside the Schwarz structure.

Figure 2 illustrates the effect of the parameters L and t on the final electrode geometry for a Gyroidal structure. A lattice size (L) of 4 mm means that the structure repeats itself every 4 mm in all directions. Hence, the lower the L, the higher the surface area. When increasing t, the strut size is reduced and consequently, the void fraction or porosity is raised. The exact mathematical relations between surface area and lattice size L, and between void fraction and t are shown in Figures S1a and S1b, Supporting Information, respectively. Also note that for Gyroids and Fischer–Koch structures, multiplying the void fraction ϕ by the lattice size L gives strut size $s = L\cdot\phi$. For Schwarz structures, this is valid only for the channel strut size, but not for the small struts connecting the channels.

The structures shown in Figure 2a have the same t parameter, corresponding to the same porosity of 70%. However, since they have different periodicities (L = 1 and 6 mm, respectively), they also have different strut sizes (0.3 and 1.8 mm, respectively) and different specific surface areas (29.8 and 6.1 $cm^2\ cm^{-3}$, respectively). The structures shown in Figure 2b have the same periodicity of 4 mm, but a different t parameter (0 and 0.8, respectively). As a consequence, not only the strut sizes are different (2 and 0.9 mm, respectively), but also the porosities (50 to 77%, respectively) and the specific surface area (10.0 and 7.9 $cm^2\ cm^{-3}$, respectively). Since bubble entrapment and gas evacuation can be expected to vary according to both parameters, we have chosen for our experimental campaign a systematic set of TPMS structures and parameters, shown in **Table 1**.

The main objective of this paper is first of all to demonstrate the performance enhancement of using such 3D printed electrodes during AWE, and second to link this enhancement to the underlying variations in structural geometry by assessing gas evacuation under forced electrolyte flow conditions.

2. Results and Discussion

2.1. Geometrical and Structural Characterization of 3D Printed TPMS Electrodes

Results for all geometrical (electrochemical active surface area [ECSA]) and structural (porosity) measurements have been included in Table 1, and are summarized in **Figure 3** as well.

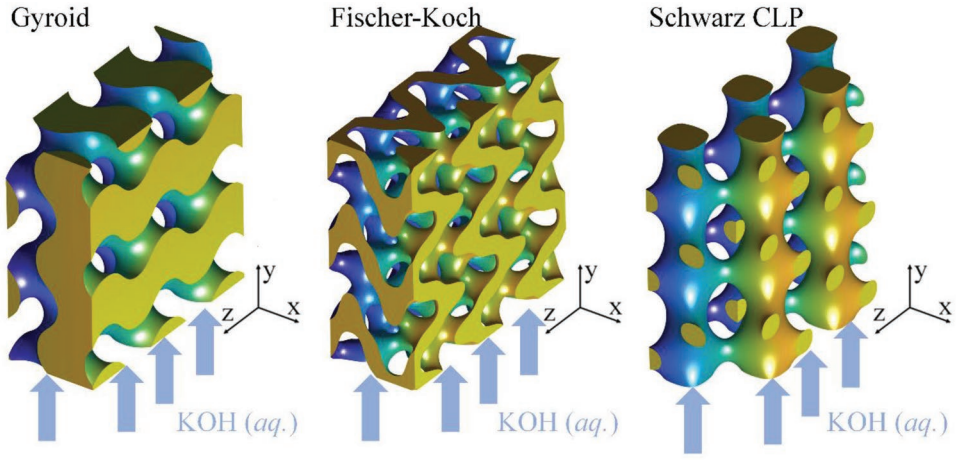

Figure 1. Examples of triply periodic minimal surfaces (TPMS) geometries. All of them contain a lattice size L of 8 mm and a t parameter of 0.26. Arrows indicate the direction of forced electrolytic flow.

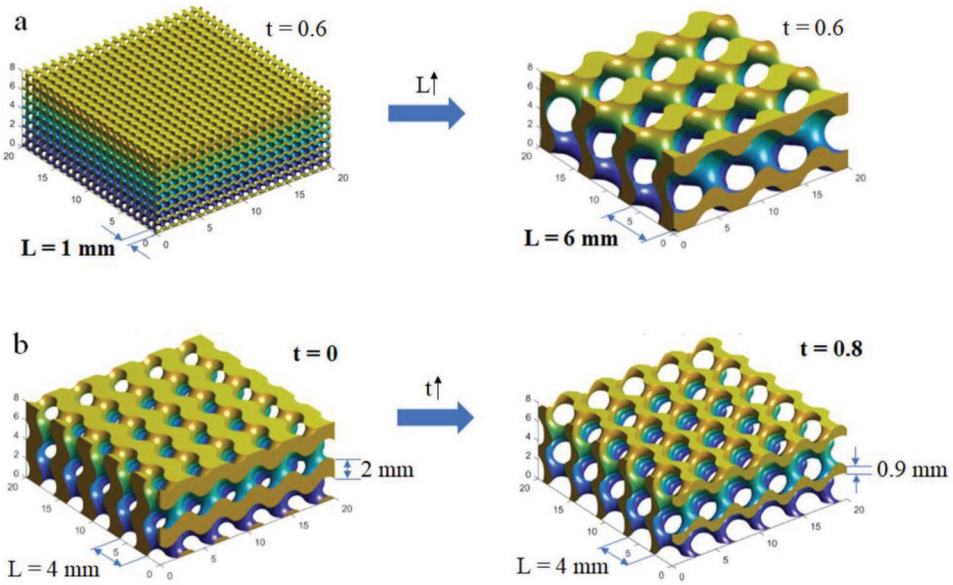

Figure 2. Gyroidal electrode geometries with different structural parameters: a) $L = 1$ and 6 mm at $t = 0.6$; b) $t = 0$ and 0.8 at $L = 4$ mm.

Porosity was lower than expected for all the cases, mainly due to the thickening of the strut, inherent from the LBM process. Briefly, when the laser beam is scanning a strut, the surrounding powder heats up due to thermal diffusion, enlarging the melting pool and thickening the strut.[14] It is shown that, generally, the deviation from the expected value is higher for lower expected porosities. Concerning the surface area, the measured value is always higher than the theoretical one. This is an expected result, since the theoretical value considers a perfectly flat surface, not accounting for the roughness. It is intrinsic to SLM that unmelted particles coming from the initial metallic powder adhere to the surface, increasing surface area (Figure S3, Supporting Information). This happens because there is partial melting of boundary particles and also an important thermal diffusion between solidified metal underneath and loose particles due to the big difference in temperature.[15] Strategies to remove powder particles attached to the surface include mechanical milling and/or polishing,[16] electrochemical polishing,[17] and a combination of abrasion and electrochemical polishing.[18] The roughness factor (ratio between real surface and completely flat one) decreases with surface area, starting at 6 and going to 3, with 4 being the average value for our 3D printed structures. Regarding strut porosity, values were in the range of 0.5–1.6%, which is in agreement with the literature. To illustrate, another study found porosities between 0.01% and 1.73% for SLM-printed Inconel 625 structures, depending on strut diameter (200–1000 µm) and angle (20–90°).[19] The exception here is the Gyroid-shaped electrode with $L = 2$ mm and $t = 0.8$, with a strut porosity of 6%. This difference may be related to printing parameters such as laser power (P), beam diameter (S), and scanning speed (V). A study shows that low volume energy density ($P/[S \cdot V]$) is related to high porosities of up to 7%.[20]

2.2. Electrochemical Performance of 3D Printed TPMS Electrodes

Polarization curves have been summarized in **Figure 4** for two series of structures with similar measured ECSA values, both at natural convection (left) and forced electrolytic flow (right).

Table 1. Structural and geometrical characteristics of selected 3D printed triply periodic minimal surface (TPMS) electrodes.

TPMS type	L [mm]	t	Theoretical [measured] porosity [%]	Theoretical [measured ECSA] area [cm^2]	Measured strut porosity [%]
Gyroid	2	0.80	77 (67 ± 1)	46.9 (173.5)	6 ± 2
	2	0	50 (43 ± 1)	56.9 (225.4)	1.2 ± 0.2
	4	0	50 (46 ± 1)	32.0 (160.6)	1.6 ± 0.1
	4	1.20	90 (86 ± 1)	16.6 (95.9)	0.92 ± 0.01
Schwarz	2	0.18	61 (51 ± 1)	55.8 (169.1)	0.90 ± 0.06
	4	0.18	61 (57 ± 1)	29.5 (115.2)	0.8 ± 0.2
	4	0.26	66 (62 ± 1)	27.6 (98.7)	0.73 ± 0.03
Fischer–Koch	2	0	50 (35 ± 1)	95.4 (288.5)	1.4 ± 0.4
	4	0	50 (44 ± 1)	50.8 (191.8)	0.74 ± 0.02
	8	0.70	86 (84 ± 1)	18.1 (85.9)	0.5 ± 0.5

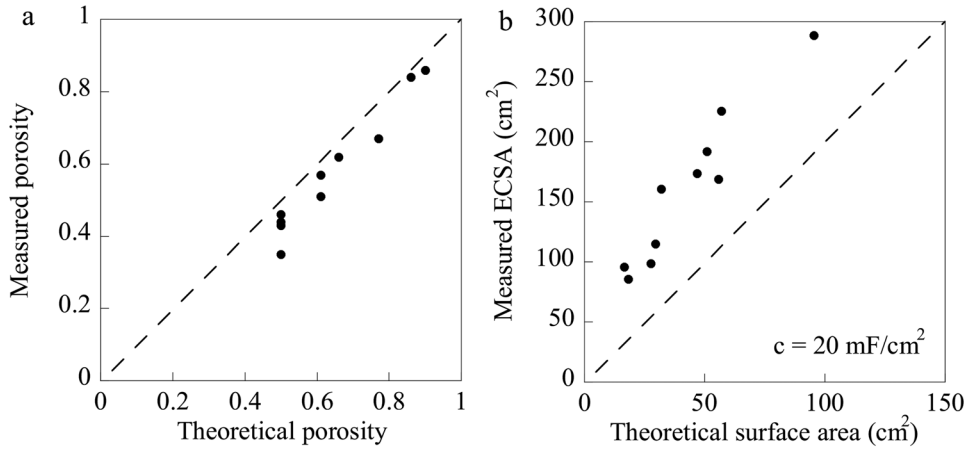

Figure 3. a) Measured porosity as a function of expected porosity. b) Electrochemical active surface area as a function of theoretical surface area.

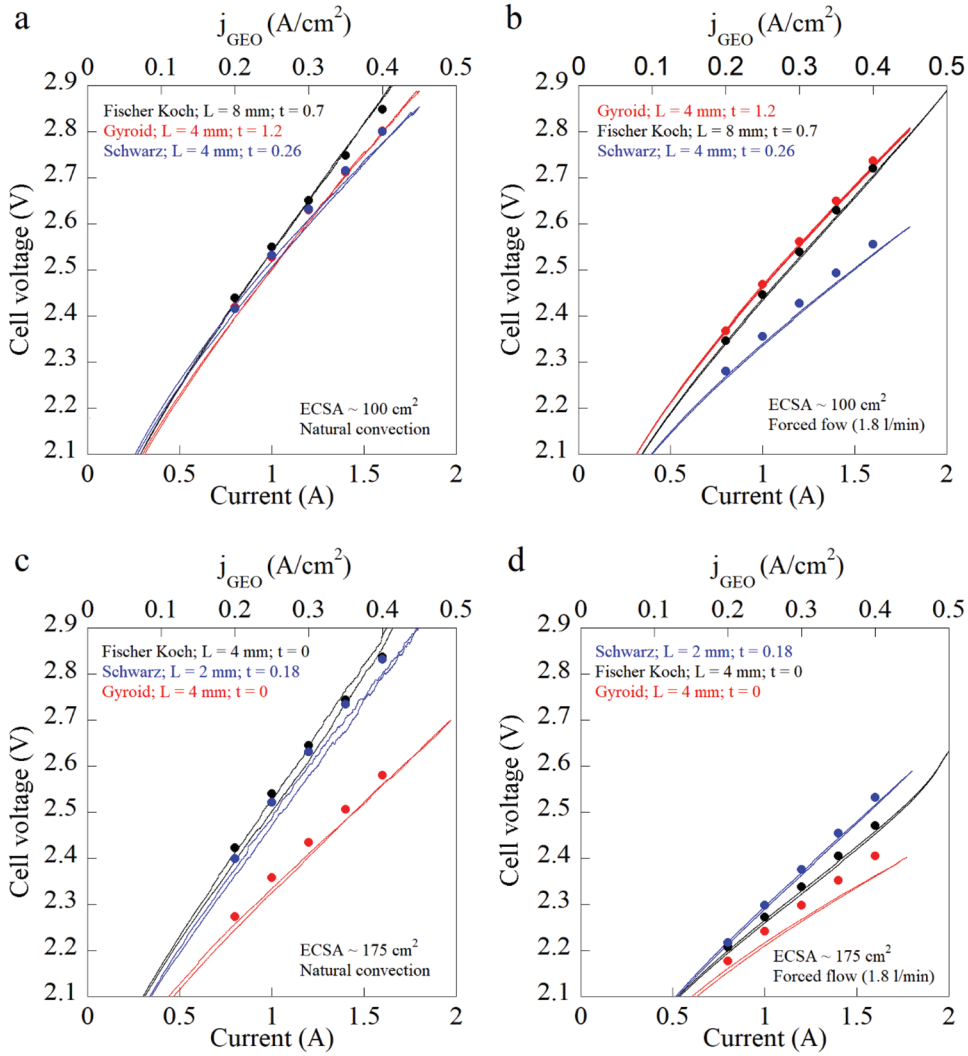

Figure 4. Evolution of cell voltage versus current for structures with an ECSA of 100 cm² at a) natural convection and b) forced flow, and for structures with an ECSA of 175 cm² at c) natural convection and d) at forced flow.

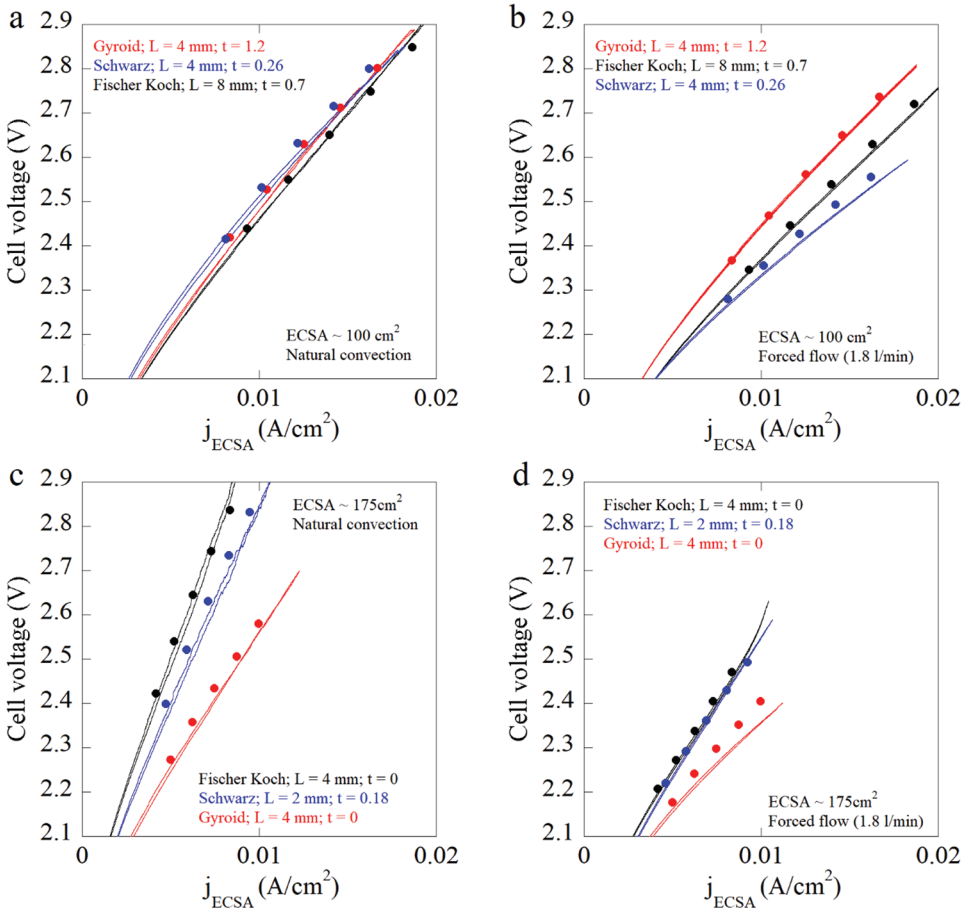

Figure 5. Evolution of the cell voltage versus electrochemical current density for structures with an ECSA of 100 cm^2 at a) natural convection and b) forced flow, and for structures with an ECSA of 175 cm^2 at c) natural convection and d) at forced flow.

It is shown that for all electrodes, the presence of a forced flow caused an increase in electrochemical performance. This is mainly due to bubble removal and confirms previous results on foam-shaped electrodes.[7] Furthermore, at natural convection, an increase in ECSA from around 100 cm^2 (Figure 4a) to around 175 cm^2 (Figure 4c) caused an important increase in performance only for the Gyroid-shaped electrode. For Schwarz and Fischer–Koch, the increase in surface area came along with an equal increase in bubble entrapment. In other words, there was no benefit in increasing the surface area because the excess surface was covered by gas bubbles. It is interesting to observe for these two electrodes at natural convection and ECSA near 175 cm^2 that the upward and downward current scans differ from one another and both present instabilities/variations. This is a result of bubbles being created and leaving the surface, altering the active surface area by its removal. The fact that this was observed for the same electrodes that did not present a performance enhancement when increasing the surface area confirms that bubble entrapment is a dominant factor in this case. The situation is different, however, at forced flow. At this condition, an increase in ECSA caused an increase in performance for all the structures. This result shows the relevance of forcing the electrolyte to circulate and remove gas from inside 3D electrodes, allowing the use of a higher percentage of the metallic surface.

Besides the global electrochemical behavior (cell voltage vs total current), it is important to have a closer look at the effect of bubble entrapment. Since water electrolysis is a heterogeneous reaction and surface matters, the polarization curves were therefore normalized by the surface area, as shown in **Figure 5**. Without the presence of bubbles, all the curves should superpose, as the electrode material is the same. The onset of all polarization curves is indeed the same (near 1.7 V), showing that the 3D printed electrodes have the same intrinsic electrocatalytic activity. However, the normalized polarization curves do not superpose, as shown in Figure 5. As a consequence, there is a difference in bubble evacuation for these structures. A forced flow helps to get rid of bubbles, decreasing the bubble coverage and therefore increasing the available surface area. Nevertheless, this effect is not always the same for all structures. For the series at 100 cm^2, they have a similar starting point at natural convection and different curves when a flow is imposed, showing different flow sensitivities. When analyzing structures with a measured surface area (ECSA) of 175 cm^2, a lower current density is observed when compared to the ones obtained for structures with a measured surface area of 100 cm^2, as a consequence of a higher bubble entrapment. In summary, an increase in ECSA usually comes along with an increase in bubble entrapment. What allows to fully

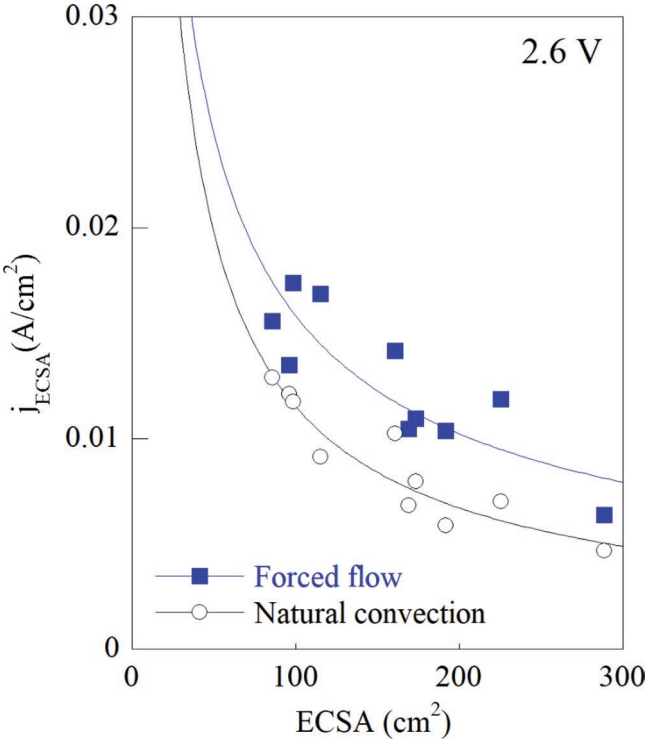

Figure 6. Electrochemical current density as a function of surface area at a constant voltage of 2.6 V.

benefit from the higher surface area is the forced electrolyte flow. This promotes bubble release, thereby making the whole surface area available again for reaction so that it approaches its intrinsic ECSA value.

In this respect, some general trends are shown in **Figure 6**. At a constant cell voltage of 2.6 V, it is shown that the current density increases with the flow as a consequence of gas removal. An alternative way of seeing this effect is to look at the Ohmic resistance ($\partial V/\partial A$). The advantage of this method is that it does not depend on the cell voltage or current chosen. Flow caused a reduction of at least 30% in Ohmic resistance when going from natural convection to a vertical velocity of 0.36 m s^{-1} for most of the electrode geometries. Furthermore, as the ECSA increases, there is a decrease in current density as a consequence of a higher bubble coverage. Finally, the curves for natural convection and forced flow seem to be diverging with ECSA, meaning that flow sensitivity is higher at higher surface areas.

2.3. Simulation of Electrolyte Flow inside 3D Printed TPMS Electrodes

Looking at the results from the CFD simulations (**Figure 7**), it is shown that the different electrode geometries create different flow patterns, and that these patterns can be related to the pressure drop along the flow direction (Figure S5, Supporting Information). Structures such as Gyroids and Fischer–Koch, with the same symmetry in all directions, cause flow mixing in the lateral direction and therefore an increase in pressure drop at constant vertical velocity. This mixing can be beneficial for processes such as desalination, where water needs to cross a separator and mixing in a flow-by cell can deviate the flow and force it against the separator, improving the mass transport. However, in the case of water electrolysis, the main objective is to get rid of bubbles as fast and as effectively as possible. As a consequence, lateral mixing may promote the coalescence of bubbles. For this case, structures able to channel the flow and reduce pressure drop will be privileged. Since the Schwarz geometry presents a different symmetry for one axis, it can guide the flow in the vertical direction, reducing pressure drop. The flow rate imposed during the experiments was in

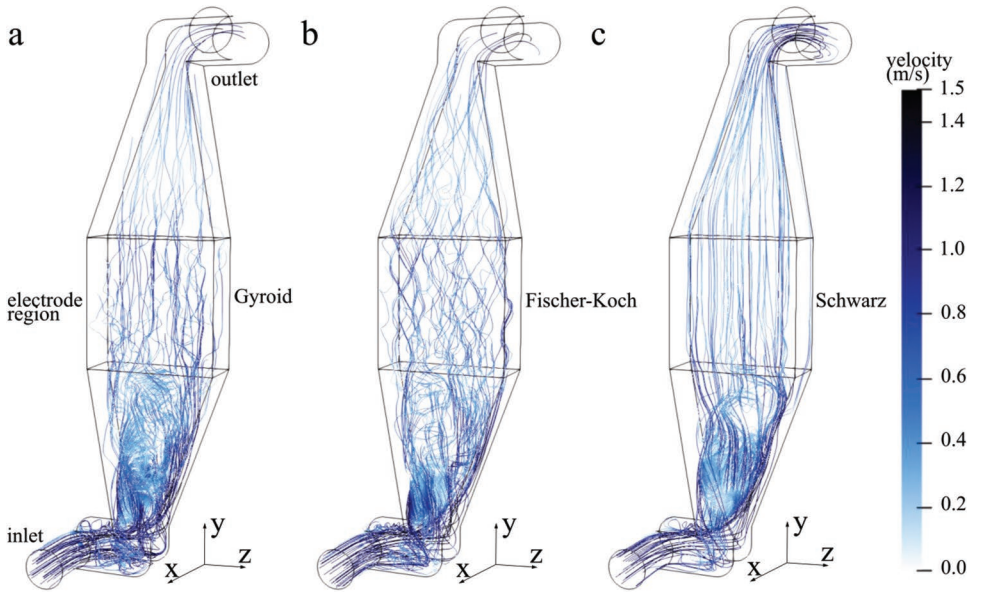

Figure 7. Velocity streamlines for structures with the same theoretical surface area (32 cm^2) and porosity (61%): a) Schwarz: $L = 4$ and $t = 0.18$; b) Gyroid: $L = 3.94$ and $t = 0.34$; c) Fischer–Koch: $L = 6.5$ and $t = 0.25$.

the range of 0.4–1.8 L min^{-1}, representing a Reynolds number between 50 and 1600, depending on the structure. For a flow inside a pipe, normally a Reynolds number close to 2000 is considered to be the transition value between laminar and turbulent regime.[21] Even though the transition Reynolds value is unknown for TPMS geometries, it is reasonable to estimate that at a Reynolds number below 1600 the flow is at a laminar regime. At laminar flow, there are different regimes defined by their governing equations: Darcy, weak inertia, and Forchheimer (strong inertia). The latter was used for Re >>1, which happens to be the case for the flow inside the analyzed structures.[22] Applying the Forchheimer equation (Equation (8)) to the plot shown in Figure S5, Supporting Information, the obtained permeability values for Schwarz, Gyroid, and Fischer–Koch are 0.08, 0.026, and 0.027 m^2. For the friction factor, the estimated values are 4.1, 16.9, and 19.3, respectively. In other words, for structures with the same surface area (32 cm^2) and porosity (61%), there are intrinsic differences due to the differences in geometries. Schwarz intrinsically has a permeability that is about three times higher than the two others and a friction factor about four to five times lower. This is a consequence of the flow channeling. Between Gyroids and Fischer–Koch, they both cause flow mixing in the x–z plane but even if permeabilities values are close, the friction factor is about 15% higher for Fischer–Koch. This analysis covers intrinsic properties when comparing structures with same surface and porosity, but different geometries. Nevertheless, these properties depend on the chosen periodicity (L) and t factor, consequently, they should be analyzed carefully case by case.

2.4. Electrochemical Performance of 3D Printed TPMS Electrodes as a Function of Electrolyte Flow

Flow sensitivity at the highest production rate studied here (1.6 A) is shown in **Figure 8** for the two electrode series with similar ECSA. For this comparison, natural convection is used as a baseline. In other words, the cell overpotential at 1.6 A is normalized by the value found at natural convection. This gives 100% at natural convection and as the flow increases, there is a decrease in the relative overpotential. The first important observation is that all the electrodes are flow sensitive and flow alone can cause a reduction of more than 20% in cell overpotential. Furthermore, the sensitivity becomes more important as the ECSA increases, confirming the observation made previously when analyzing Figure 6. At 100 cm^2 of surface, the relative overpotential reduction ranges from 4% to 16%, while for 175 cm^2, it is between 13% and 23%. Having a closer look at Figure 8a, it is shown that there is a difference in sensitivity for the different structures, with Schwarz being the most sensitive. It could be argued however that the observed difference does not arise from differences in geometry, but differences in porosity. In this series, the higher the porosity, the less flow-sensitive the electrode was. Porosity can indeed play a role in flow sensitivity. It could be supposed that at a constant ECSA, structures with higher porosities have less bubble entrapment and as a consequence, are less sensitive to flow. To deepen the understanding of the phenomena and confirm that there are intrinsic differences in flow sensitivity caused by the electrode geometry, structures with similar ECSA (160.6–191.8 cm^2) and porosities (44–51%) should be compared. This comparison is shown in Figure 8b. For the Gyroid and Fischer–Koch, they have the same properties, yet, the flow sensitivity is higher for Fischer–Koch. The Schwarz-shaped electrode has a sensitivity that is comparable to the one for Fischer–Koch, even though its porosity is higher. Consequently, Schwarz can potentially be the most flow-sensitive if structures with the same porosity and ECSA are compared.

3. Conclusion

In this work, 3D printed Inconel electrodes were tested and simulated. It was first shown that it is feasible to print electrodes

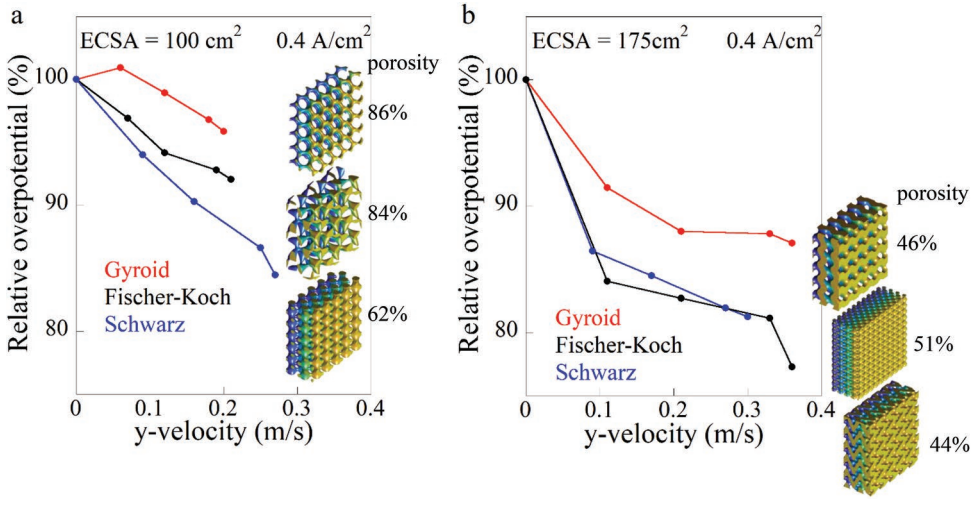

Figure 8. Flow sensitivity at projected current density of 0.4 A cm^{-2} for: a) Structures with a measured ECSA around 100 cm^2 (Gyroid: L = 4 mm, t = 1.2; Fischer–Koch: L = 8 mm, t = 0.7; Schwarz: L = 4 mm, t = 0.26); b) Structures with a measured ECSA around 175 cm^2 (Gyroid: L = 4 mm, t = 0; Fischer–Koch: L = 4 mm, t = 0; Schwarz: L = 2 mm, t = 0.18).

and use them in an alkaline electrolyzer. This proof of concept opens new possibilities for electrode geometries, combining high surface area with effective gas removal. Furthermore, it was shown that forced electrolytic flow is an important tool to get rid of bubbles and liberate the electrode surface, increasing process performance by reducing the overpotential by up to 20%. Moreover, it was shown that at the length scale used here, there was a compromise between surface area and bubble coverage. It was also shown that intrinsically, for structures with the same surface area and porosity, geometries that channel the flow and avoid mixing in the transversal plane present lower pressure drop, higher permeabilities, and lower friction factor. Finally, when looking at flow sensitivity, it was shown that structures present different sensitivities depending on the surface area, porosity, and geometry. The sensitivity was higher for electrodes with higher surface areas. Schwarz-shaped electrodes are potentially the best of the analyzed structures, as it has intrinsically a high permeability and an important flow sensitivity.

4. Experimental Section

The electrolytic solution was 1.0 M potassium hydroxide (KOH), prepared by dissolving KOH pellets (KOH > 85%, VWR chemicals) in deionized water (18.2 MΩ cm, Sartorius Arium 611) at room temperature and atmospheric pressure. Room temperature was chosen because the idea was to use natural convection (no forced flow) as a baseline. Since heating in the experimental cell was done at the reservoir level and there were heating losses between the reservoir and the cell, the temperature inside the cell during natural convection would be lower than inside the reservoirs. Details about the experimental setup can be found in a previous publication[7] and in Figure S2, Supporting Information. The cell contains the following parts: two end-plates with fittings for inlet and outlet of electrolyte; two nickel plate (>99.5%, Alfa Aesar) current distributors to ensure removal/supply of electrical charge; two PTFE electrode housings to accommodate the electrodes and promote sealing; and a Fumasep FAA-3-PK anion exchange membrane (130 µm thickness). Between each one of these parts, an ethylene propylene diene monomer layer ensured sealing and prevented mechanical wear. The electrodes had dimensions of 2 × 2 × 0.8 cm (length, width, thickness) and some of them are shown in Figure S3, Supporting Information. The electrolytic flow was controlled by gear pumps (GJ-N25.FF3S.A, Micropump) and measured by flow transmitters (Honsberg, model LABO-MID1-I/U/F/C). The electrolytic reservoirs were made of 316l stainless steel. To ensure sealing, the cell was pressed using six screws with a torque of 3 Nm each.

Current scans from 0–2 A were performed with a scan rate of 0.1 A s^{-1} with the help of a Solartron Modulab XM potentiostat equipped with a 20 A booster, and complemented with 5 min of galvanostatic experiments at geometrical current densities of 0.20, 0.25, 0.30, 0.35, and 0.40 A cm^{-2}.

In order to have a better understanding of the electrolyte flow behavior inside the 3D electrodes, numerical simulations were performed as well. Regarding the numerical setup, the incompressible Navier–Stokes equations for a single-phase flow through the cell were solved. Both bubble size and density might strongly affect the electrolyte flow behavior, but such highly challenging gas/liquid dual phase CFD was outside the scope of the current work. The equations were solved using the finite element method implemented in the open-source MigFlow solver.[23] A half-cell was modeled using a marching cubes method for the meshing of the TPMS geometry in the context of GMSH meshing software. The physical dimensions of the cell were: circular fluid inlet/outlet with a 3 mm radius, 2 × 2 × 0.8 cm electrode. The tetrahedral mesh had an element size in the order of 0.25 mm outside the electrode region and 0.1 mm inside it. These values were determined after a mesh sensitivity analysis. For the simulations, an average fluid velocity was imposed at the half-cell inlet and the pressure was set at 1 atm at the outlet. Solution density and dynamic viscosity were set at 1260 kg m^{-3} and 10^{-3} Pa s, respectively.[24] The pressure drop inside the cell was estimated as a function of velocity. Using Paraview software, one could visualize streamlines and velocity or vorticity contours as a post-processing step. For simplicity, the anion exchange membrane was approximated by a wall with no fluid crossing.

Reynolds number was estimated as:

$$Re = \frac{\rho \cdot \bar{v} \cdot l}{\mu} \tag{5}$$

with ρ the fluid density, $\bar{v}$ the average vertical velocity, μ the dynamic viscosity, and l the characteristic length defined as:

$$l = \frac{4 \cdot V}{A} \tag{6}$$

with V the area of the fluid domain inside the electrode region and A the electrode surface area.[25] The Fanning friction factor was calculated as:

$$f = \frac{2 \cdot \Delta P}{\rho \cdot (\bar{v})^2} \tag{7}$$

with ΔP the pressure drop. For permeability, a fit using the Forchheimer equation was done in the pressure drop versus vertical velocity plot. This equation was defined as:

$$\frac{-dP}{dx} = \frac{\mu \cdot \bar{v}}{k_1} + \rho \cdot \beta \cdot \bar{v}^2 \tag{8}$$

with k_1 the permeability and β the drag coefficient.

Electrodes were made by LBM of a Ni-based Inconel 625 alloy (Ni ≈ 60%, Cr ≈ 22%, Mo ≈ 9%, Fe ≈ 4%, Nb ≈ 3%).[26] This alloy was simply chosen for ease of fabrication, allowing to use an already existing LBM protocol. This composition might not be the ideal electrocatalyst composition for AWE, but since this work was intended to concentrate on the structural aspects of the electrode's geometrical design, the results can still be expected to be highly relevant for other electrode compositions as well.

The ECSA of each electrode was measured using the capacitance method: cyclic voltammetries (CVs) with different scan rates (50, 100, 150, 200, 250, 300, 350, and 400 mV s^{-1}) were applied in a range of 50 mV around open circuit potential to estimate the capacitive current. This current was measured by taking half of the difference between the anodic current and the cathodic one. The slope of the plot of capacitive current against the CV scan rate gave out capacitance. To find the ECSA, the capacitance was divided by a specific capacitance of 20 µF cm^2, as this value was reported recently in the literature[27] and also measured at the lab.[7] This measurement was made at room temperature, 1 M KOH, using a Pt counter electrode, and an Ag|AgCl sat. reference electrode. More details about the capacitance method can be found in ref. [28] and some representative measurements are given in Figure S4, Supporting Information.

Porosity was measured by hydrostatic weighting (ISO 18754:2020). For that, dried electrode samples were weighted (m_d). Then, the samples were completely submerged in a solution of 70% ethanol and 30% water and weighed again (m_w). The density of this solution (ρ_s) was estimated with the help of a pycnometer. Using Archimedes' principle, the volume could then be estimated:

$$V = \frac{m_d - m_w}{\rho_s} \tag{9}$$

Knowing the total dimensions of the electrode and the metallic volume, porosity could be estimated and it was averaged between the two pairs of electrodes (cathode and anode). This method allowed estimating the strut porosity as well. For that, the strut density was compared with the massive metallic density (ρ_m):

$$\rho_{strut} = \frac{m_d}{V} = \rho_m \cdot (1 - x) + \rho_{air} \cdot x \tag{10}$$

with ρ_{air} the air density (0.001225 g mL^{-1}[29]) and x the porosity. The density for Inconel 625 was considered to be 8.44 g mL^{-1} (value from the manufacturer).

Supporting Information

Supporting Information is available from the Wiley Online Library or from the author.

Acknowledgements

The authors gratefully acknowledge financial support from the European Commission through the H2020 Project "NexTAEC" (Materials for Next Generation Alkaline Electrolyzers), under contract no. 862509.

Conflict of Interest

The authors declare no conflict of interest.

Data Availability Statement

The data that support the findings of this study are available from the corresponding author upon reasonable request.

Keywords

alkaline water electrolysis, bubble removal, forced electrolytic flow, three-dimensional printed electrodes

Received: September 9, 2022
Revised: October 13, 2022
Published online:

[1] International Energy Agency. Global Energy Review 2021/International Energy Agency(IEA), France: IEA, April, **2021**.
[2] Y. Li, T. Zhang, J. Ma, X. Deng, J. Gu, F. Yang, M. Ouyang, *Mater. Today Phys.* **2022**, *22*, 100606.
[3] J. Proost, *Int. J. Hydrogen Energy* **2019**, *44*, 4406.
[4] N. Guillet, P. Millet, in *Hydrogen Production: Electrolysis*, Wiley, New York **2015**, pp. 117–166.
[5] M. Koj, J. Qian, T. Turek, *Int. J. Hydrogen Energy* **2019**, *44*, 29862.
[6] F. Yang, M. J. Kim, M. Brown, B. J. Wiley, *Adv. Energy Mater.* **2020**, *10*, 2001174.
[7] F. Rocha, R. Delmelle, C. Georgiadis, J. Proost, *J. Environ. Chem. Eng.* **2022**, *10*, 107648.
[8] T. Kou, S. Wang, R. Shi, T. Zhang, S. Chiovoloni, J. Q. Lu, W. Chen, M. A. Worsley, B. C. Wood, S. E. Baker, E. B. Duoss, R. Wu, C. Zhu, Y. Li, *Adv. Energy Mater.* **2020**, *10*, 2002955.
[9] A. Mertens, O. Dedry, D. Reuter, O. Rigo, J. Lecomte-Beckers, in *Proc. of the 26th Annual Int. Solid Freeform Fabrication Symp*, (Ed.: D. L. Bourell), University of Texas at Austin, Austin **2015**, p. 1007.
[10] P. K. Gokuldoss, S. Kolla, J. Eckert, *Materials* **2017**, *10*, 672.
[11] N. Thomas, N. Sreedhar, O. Al-Ketan, R. Rowshan, R. K. A. Al-Rub, H. Arafat, *Desalination* **2018**, *443*, 256.
[12] S. Yu, J. Sun, J. Bai, *Mater. Des.* **2019**, *182*, 108021.
[13] N. Sreedhar, N. Thomas, O. Al-Ketan, R. Rowshan, H. Hernandez, R. K. A. Al-Rub, H. A. Arafat, *Desalination* **2018**, *425*, 12.
[14] S. Van Bael, G. Kerckhofs, M. Moesen, G. Pyka, J. Schrooten, J. P. Kruth, *Mater. Sci. Eng. A* **2011**, *528*, 7423.
[15] M. Fousová, D. Vojtěch, K. Doubrava, M. Daniel, C.-F. Lin, *Materials* **2018**, *11*, 537.
[16] S. Milton, A. Morandeau, F. Chalon, R. Leroy, *Proc. CIRP* **2016**, *45*, 127.
[17] S. Jain, M. Corliss, B. Tai, W. N. Hung, *Procedia Manuf* **2019**, *34*, 239.
[18] C. Zhao, N. Qu, X. Tang, *J Manuf Process* **2021**, *64*, 1544.
[19] M. Leary, M. Mazur, H. Williams, E. Yang, A. Alghamdi, B. Lozanovski, X. Zhang, D. Shidid, L. Farahbod-Sternahl, G. Witt, I. Kelbassa, P. Choong, M. Qian, M. Brandt, *Mater. Des.* **2018**, *157*, 179.
[20] I. Koutiri, E. Pessard, P. Peyre, O. Amlou, T. De Terris, *J. Mater. Process. Technol.* **2018**, *255*, 536.
[21] J. Iyer, T. Moore, D. Nguyen, P. Roy, J. Stolaroff, *Appl. Therm. Eng.* **2022**, *209*, 118192.
[22] J. Santos, T. Pires, B. P. Gouveia, A. P. G. Castro, P. R. Fernandes, *J. Mech. Behav. Biomed. Mater.* **2020**, *110*, 103932.
[23] M. Constant, F. Dubois, J. Lambrechts, V. Legat, *Comput. Part. Mech.* **2019**, *6*, 213.
[24] K. I. Kuznetsov, S. V. Skorodumov, P. P. Granchenko, *High Temp.* **2020**, *58*, 806.
[25] M. Ouda, O. Al-Ketan, N. Sreedhar, M. I. Hasan Ali, R. K. A. Al-Rub, S. Hong, H. A. Arafat, *J. Environ. Chem. Eng.* **2020**, *8*, 104289.
[26] N. Ramenatte, A. Vernouillet, S. Mathieu, A. V. Put, M. Vilasi, D. Monceau, *Corros. Sci.* **2020**, *164*, 108347.
[27] S. P. Zankowski, P. M. Vereecken, *J. Electrochem. Soc.* **2019**, *166*, D227.
[28] E. Cossar, M. S. E. Houache, Z. Zhang, E. A. Baranova, *J. Electroanal. Chem.* **2020**, *870*, 114246.
[29] A. Ulazia, J. Sáenz, G. Ibarra-Berastegi, S. J. González-Rojí, S. Carreno-Madinabeitia, *Energy* **2019**, *187*, 115938.